J Mater Sci: Mater Electron (2017) 28:10772–10779
DOI 10.1007/s10854-017-6854-1

Superparamagnetic behaviour of zinc ferrite obtained by the microwave assisted method

B. Hangai[1] · E. Borsari[1] · E. C. Aguiar[4] · F. G. Garcia[2] · E. Longo[3] · A. Z. Simões[1]

Received: 28 December 2016 / Accepted: 25 March 2017 / Published online: 8 April 2017

Abstract Magnetic $ZnFe_2O_4$ nanoparticles with magnetization saturation of 12.1 emu/g were synthesized through hydrothermal microwave method at 140 °C for 32 min. These compound is being tested in magnetic hyperthermia a promising therapeutic cancer treatment, which causes lysis of tumor cells by heating magnetic nanoparticles through an external magnetic field. X-ray diffraction reveals a single-phase $ZnFe_2O_4$ nanoparticles with well-defined structure while Raman spectroscopy reveals that at 32 min of soaking time provides the energy crystallization, causing anisotropy in the structural growth at short range causing a certain degree of order in the crystal lattice. Morphology of the powders was investigated by transmission electronic microscopy (HRTEM) which showed particle sizes with 10–25 nm of diameter being an important factor for application in magneto-hyperthermia. Magnetic parameters analyzed by means of a vibrating-sample magnetometer unit showed that these nanoparticles have great potential in magneto-hyperthermia application.

✉ A. Z. Simões
alezipo@yahoo.com

[1] Faculty of Engineering of Guaratinguetá, São Paulo State University - UNESP, Guaratinguetá, SP, Brazil

[2] Physics and Chemistry Institute, Federal University of Itajubá - UNIFEI, Itajubá, MG, Brazil

[3] Interdisciplinary Laboratory of Electrochemistry and Ceramics, LIEC - Department of Chemistry Techonology, Chemistry Institute, São Paulo State University - UNESP, Araraquara, SP, Brazil

[4] Mato Grosso do Sul State University, Cidade Universitária, UEMS, Dourados, MS, Brazil

1 Introduction

Lately, the large number of individuals with cancer has been a major concern in the global scenario [1]. Cancer cells are generated due to mutations in special genes, which are inactive in normal cells, forming the malignant or benign tumor [2, 3]. In particular liver cancer, you risk being contracted for numerous reasons, such as food intake with aflatoxins, among others [4–7]. Magnetic hyperthermia is a relatively new method to aid in the treatment of cancer and the most robust of the possibilities [8, 9]. Magnetic particles are inserted into the bloodstream and they go and bind to cancer cells. By raising the temperature to ~42 °C through an alternating magnetic field, it generates enough heat to destroy the cancerous cells. To be applied in the treatment of cancer, the behavior may be ferromagnetic or superparagnetic, the latter being preferred because it requires a less intense field [8]. The nanostructured materials have at least one of their dimensions in the order of nanometers. It has typical characteristics, such as better conductivity, better sintering rates, rapid response in sensors, among others [10]. The particle size distribution (to be applied to the capillaries [11]) as well as good dispersion should be well controlled. Nanoparticles (magnetic monodomains) are preferred to microparticles (mango multidomains) because they respond more efficiently to external fields, absorbing more energy. The material chosen for hyperthermia is zinc ferrite ($ZnFe_2O_4$), due to its high stability, heating by magnetic induction, biocompatibility and interesting physical properties [12]. In addition to having adequate magnetization saturation, the zinc ferrite obtained by a facile co-precipitation route has crystallite size of 11.04 nm, interplanar distance of 2.542, volume of 592.06 $Å^3$, Neel temperature around 9–10 K, bulk density of 4.12 gm/cm³, Fermi energy of 14.642 eV, porosity

of 23.83%, among other characteristics [13]. Its structure corresponds to normal spinel, where Zn^{+2} occupies the tetrahedral site and Fe^{+3} occupies the octahedral site, normally. Bulk $ZnFe_2O_4$ has a normal spinel structure with nonmagnetic Zn^{2+} ions in the A-site and magnetic Fe^{3+} ions in the B-sites (in two antiparallel sublattices) and can be described by the formula $(Zn^{2+})[Fe^{3+}\uparrow Fe^{3+}\downarrow]O_4$ [14]. When the interactions between the sites decrease in bulk and room temperature magnetization is of the paramagnetic type. However, when the structural inversion occurs, in which the metallic ions begin to occupy the inverted sites, the magnetic behavior changes to ferromagnetic, which is the desired magnetic behavior. This cationic rearrangement leads to the formation of two magnetic sublattices, which is responsible for the enhanced magnetization displayed when compared with normal $ZnFe_2O_4$ [14]. Considering this structural inversion, the magnetic behavior in nanoparticles of zinc ferrite observed is superparamagnetic, explained as follows: a sample of a uniaxial ferromagnet with a volume above the critical volume is divided into multiple magnetic domains, each magnetized along the D-axis, in different directions. However, when the volume is below the critical volume, the particle becomes only a single domain, with ferromagnetic alignment of all its moments in a single direction along the same direction D. There are thermal fluctuations of moments (with a variation of energy, on a microscopic scale), but to reverse the magnetization of a single domain requires a certain energy to overcome the anisotropy of the material. Making the particle small enough frees up its constraints, which allows the direction of the moments to change as an ideal paramagnet [15, 16]. The magnetic susceptibility can be equated by the Langevin equation and its magnetization is obtained by the Langevin function [17]. The ideal phase transition temperature would be between 40 and 43 °C, because it will be the working temperature [8]. With interesting magnetic behavior, spinel ferrite has been the subject of research lately, including its applications [18, 19]. As $ZnFe_2O_4$ is one of the most important spinel ferrites, numerous methods are developed for its production, such as sol–gel, hyperthermia, among others [20–25].

2 Experimental procedures

The reagents used for the synthesis were: ammonium iron (III) citrate (purity 99.5% and supplied by Vetec) and zinc acetate dihydrate (purity 99.9% and supplied by Merck). All reactants were weighted according to the previous defined stoichiometry ($ZnFe_2O_4$). The solution was obtained by dissolving ammonium iron (III) citrate and zinc acetate dehydrate with drops of nitric acid in water at 90 °C and constant mixing. Afterwards, solution had a pH of 3. The final solution was transferred into a sealed Teflon autoclave and placed in the hydrothermal microwave (2.45 GHz, maximum power of 200 W). The hydrothermal synthesis was carried out at 140 °C for 32 min with a heating rate fixed at 10 °C/min. The pressure in the sealed autoclave was stabilized at around 2.0 atm during the synthesis. The autoclave was cooled down to the room temperature inside the microwave once stipulated times were reached. The polycrystalline $ZnFe_2O_4$ nanoparticles were collected and washed with deionized water several times and then dried at 100 °C in an oven. The obtained nanoparticles were characterized by X-ray powder diffraction (XRD) using a (Rigaku-DMax/2500PC, Japan) with Cu-Kα radiation (λ = 1.5406 Å) in the 2θ ranging from 20° to 70° with 0.2 °/min. The crystallite size (d) was calculated using Scherrer equation $d = k\lambda/\beta\ cos\ \theta$, where k is constant, λ is wavelength of X-rays and β is the full width at half maximum (FWHM) for (311) reflection measured from slow scan where θ is the diffraction angle of the main peak. The Rietveld analysis was performed with the Rietveld refinement program DBWS-941 1. The profile function used was the modified Thompson-Cox-Hasting pseudo-Voigt, in which η (the lorentzian fraction of the function) varies with the Gauss and Lorentz components of the full width at half maximum. Raman spectra were collected (Bruker RFS-100/S Raman spectrometer with Fourier transform). A 1064 nm YAG laser was used as the excitation source, and its power was kept at 150 mW. Specimens for TEM were obtained by drying droplets of as-prepared samples from an ethanolic dispersion which had been sonicated for 5 min onto 300 mesh Cu grids. TEM images and selected area diffraction (SAED) patterns were then taken at an accelerating voltage of 200 kV on a Philips model CM 200 instrument. The powders particle size distributions were determined by the hydrodynamic particle size technique using liquid media. In order to measure dc magnetic field, a Hall probe was employed. Magnetization measurements were realized through vibrating-sample magnetometer (VSM) from Quantum Design™. The N_2 sorption measurement was performed using Micromeritics ASAP 2010 at 77 K.

3 Results and discussion

XRD patterns of $ZnFe_2O_4$ nanopowders synthesized at 140 °C for 32 min is shown in Fig. 1. Diffraction peaks can be indexed mainly with $ZnFe_2O_4$ according to the powder data of JCPDS card no. 22-1012. These peaks revealed that the spinel ferrite crystallites show the characteristic reflections of spinel cubic crystal structure of ferrite belonging to the polar *Fd-3m* space group which indicates that the hydrothermal technique was successfully used to produce almost pure crystalline nanoparticles. Besides that, no

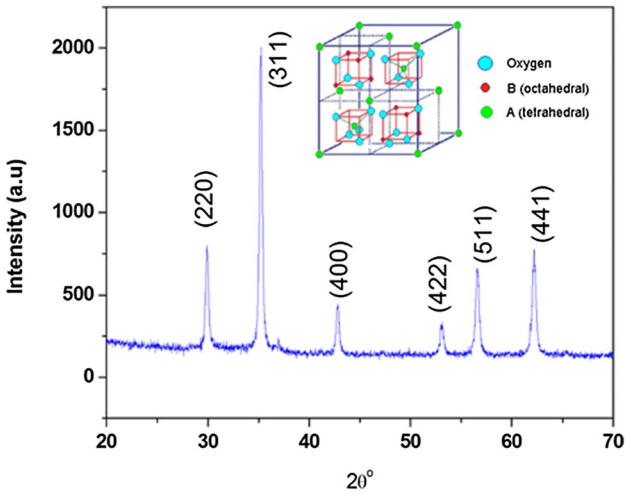

Fig. 1 XRD pattern for $ZnFe_2O_4$ powders synthesized at 140 °C for 32 min using the microwave assisted hydrothermal method. Inset shows the crystal structure of inverted spinel ferrite

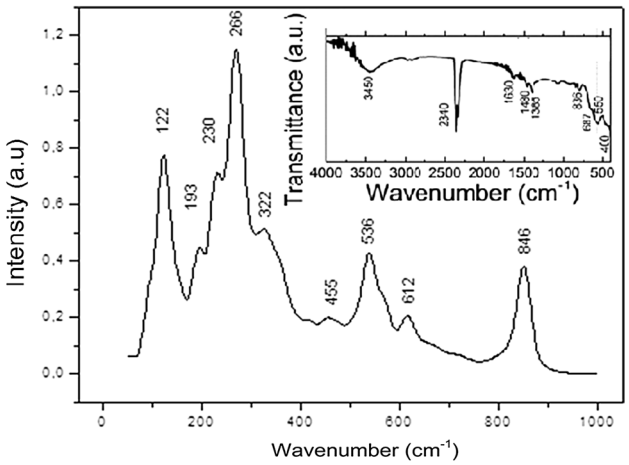

Fig. 2 Raman spectra of a $ZnFe_2O_4$ nanoparticle synthesized at 140 °C for 32 min using the microwave assisted hydrothermal method. Inset shows the FT-IR spectra of a $ZnFe_2O_4$ nanoparticle synthesized at 140 °C for 32 min

impurities phases were detected in addition to the major phase revealing that the hydrothermal microwave method (HTMW) process allows the formation of a single phase at reduced temperature and soaking time. Small variations observed in the XRD pattern can be associated with distortions in the lattice which possibly can be associated with the rapid formation kinetic of spinel ferrite powders due to the influence of microwave radiation during the HTMW processing. The X-ray pattern displaying sharp and well-resolved diffraction peaks proves that the products are in good crystallinity. Average crystallite sizes were calculated by using XRD data by measuring the *FWHM* for most intense characteristic (311) peak with the help of the Scherer formula resulting in a value of 30.4 nm.

Raman scattering has proven to be a valuable technique to obtain information about local structures within materials. Raman spectra of the $ZnFe_2O_4$ nanoparticle obtained in the hydrothermal reator is illustrated in the inset of Fig. 2 revealing a spinel phase with a cubic structure that belongs to the space group O_h^7 (*Fd-3m*). Although the full unit cell contains 56 atoms (Z = 8), the smallest Bravais cell only consists of 14 atoms (Z = 2): As a result, the factor group analysis predicts the following modes in $ZnFe_2O_4$ spinel:

$$A_{1g}(R) + E_g(R) + F_{1g} + 3F_{2g}(R) + 2A_{2u} + 2E_u + 4F_{1u}(IR) + 2F_{2u}$$

There are five first-order Raman active modes ($A_{1g} + E_g + 3F_{2g}$), and all these modes were observed at ambient conditions, as shown in the inset of Fig. 2. In the cubic spinels including ferrites, the modes at above 600 cm^{-1} mostly correspond to the motion of oxygen in tetrahedral AO_4 groups [26], so the mode at 612 cm^{-1} can be reasonably considered as A_{1g} symmetry. The other low frequency modes represent the characteristics of the octahedral sites (BO_6). The three first-order Raman modes at 266, 536 and 846 cm^{-1} exhibit the broad characteristics. Nevertheless, the origin of the broadening of those firstorder modes remains unclear. We suposse that the fast structural organization of $ZnFe_2O_4$ powder processed in HTMW can be related to the heating process which occurs from the interior to the surface. The microwave energy is transformed into heat through the interaction between molecules and atoms with the electromagnetic field. This interaction results in an internal and volumetric heating of the powders which promotes the formation of temperature gradients and heat flows [27]. Raman results are in agreement with XRD data; therefore, small changes observed in the spectra can be associated with the preparation method, average crystal size and the degree of structural order. The X-ray diffraction of this sample exhibits a slightly inverted structure [28], which implies that a certain amount of disorder of the Zn and Fe cations occurs in the tetrahedral and octahedral sites. Hence, the vibrations relating to these two types of cations at the same site may display two separated first-order Raman modes. If the two modes have very close vibrational frequencies, an overlapped broad peak with their average value should be observed. In this slightly inverted $ZnFe_2O_4$ spinel, Zn and Fe ions distribute at the same atomic crystal site, either the tetrahedral or octahedral, and result in the corresponding vibrations with different frequencies. Since these two vibrations have very close wavelengths, the three broad first-order Raman spectroscopic peaks were observed in this $ZnFe_2O_4$ spinel (Fig. 2). This is a plausible interpretation for the three observed broad first order Raman modes. Inset of Fig. 2 shows the FT-IR spectra of crystalline $ZnFe_2O_4$ powders derived from the hydrothermal reaction. The broad band at

3000–3600 cm^{-1} is the result of antisymmetric and symmetric stretching of H_2O and OH^{-1} bond groups, while a band at 1630 cm^{-1} corresponds to the bending vibrations of H_2O [29–31]. Specifically, strong absorptive peaks at 400–600 cm^{-1} are attributed to the Fe–O stretching and bending vibration which is characteristic of octahedral FeO_6 groups in the perovskite compounds. The formation of a perovskite structure can be confirmed by the presence of metal–oxygen band [32, 33]. Residual water and hydroxy groups are usually detected in the as grown samples and further heat treatment is necessary for their elimination. It is well known that the hydroxylation of metal ions and the deprotonation can be accelerated by raising the solution temperature or pressure [34]. In hydrothermal-microwave processing the high frequency electromagnetic radiation interacts with the permanent dipole of the liquid (H_2O), which initiates rapid heating from the resultant molecular rotation and permanent or induced dipoles in the dispersed phase cause rapid heating of the particles which results in a reaction temperature in excess of the surrounding liquid-localized superheating [35, 36]. Out of the two bands the high frequency (υ_1) band is attributed to the tetrahedral metal–oxygen bond and second frequency (υ_2) band to the octahedral metal–oxygen bond corresponding to: (1) Me_T–O–Me_O stretching vibration 600–550 cm^{-1} (2) $Me_O \leftrightarrow O$ stretching vibration 450–385 cm^{-1} here O is oxygen, Me_O is metal in the octahedral site and Me_T in the tetrahedral site. The metal–oxygen absorption bands (1) and (2) are pronounced for all spinel structures and essentially for ferrites, which are also seen in these samples. FT-IR spectral data of all the ferrite samples prepared by these methods are found to show two peaks in the range 578–564 cm^{-1} and 472–443 cm^{-1} which are in agreement with the reported value [37]. Typical band characteristics of carbonate traces could be attributed to adsorbed water due to the contact of the sample with the environment near 1500 cm^{-1}.

The FEG-SEM (analysis by Scanning Electron Microscope in Faculty of Engineering of Guaratinguetá—FEG) images exhibit (Fig. 3) agglomerated bunch of square shaped nanoparticles. The small size of nanoparticles leads to high agglomeration because of its high surface energy [38]. It is difficult to determine the exact size of the particle using FEG-SEM because most of the particles are agglomerated [39]. In the hydrothermal process, the ''dissolution and crystallization'' process can be utilized to describe the hydrothermal reaction [40]. During the hydrothermal treatment, Zn^{2+} and Fe^{3+} hydroxides were dissolved and react at high temperatures and pressures, and then precipitated as insoluble ceramic oxide particles from the supersaturated hydrothermal fluid. If the temperature and pressure conditions are carefully maintained during the duration of the experiment, neither etching of cubic ferrite crystals nor

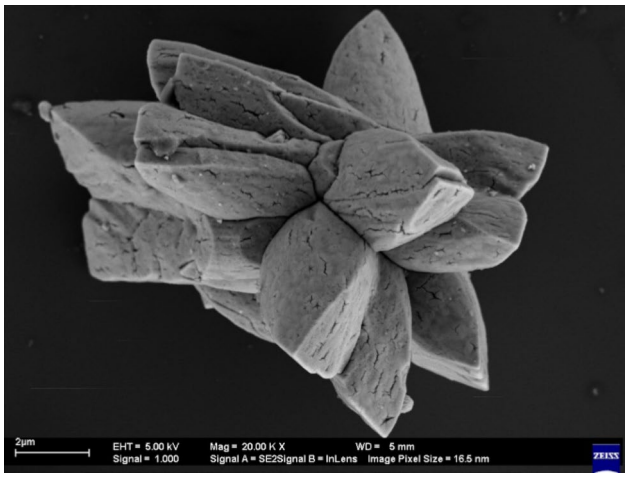

Fig. 3 FEG-SEM images of $ZnFe_2O_4$ agglomerated particles synthesized at 140 °C for 32 min using the microwave assisted hydrothermal method

the formation of a second phase is observed. Therefore, the dissolution and crystallization process continued in supersaturated fluid in such a way that the system was self-stabilizing. We conjecture that the dissociation of zinc and iron hydroxide and the formation of ionic complexes might prevent the growth of crystallites and limit the size of particles to the nanometric range. The agglomeration process was attributed to Van der Waals forces. To reduce the surface energy, the primary particles have a tendency to form nearly spherical agglomerates, in a minimum surface to volume ratio [41]. This type of grain structure is common in oxide, ferrite and titanate ceramics [42–49] which is a result of an abnormal/discontinuous grain growth and also called an exaggerated grain growth. In abnormal growth, some grains grow faster than others grains with increasing sintering temperature. Abnormal grain growth may results from: (1) the existence of second phase precipitates or impurities, (2) materials with high anisotropy in interfacial energy and (3) materials with high chemical equilibrium [50]. In hydrothermally derived $ZnFe_2O_4$ which crystallizes in a cubic structure it can be assumed that the abnormal grain growth comes from factor (1) and (3) due the existence of two-phase structure. At intermediate temperatures, a higher degree of agglomeration was noted which could be due to the favored nucleation process at higher OH^- concentration with no separation of particles which is due to a low reaction temperature. The random aggregation process between the small particles can be related to an increase in effective collision rates between small particles by microwave radiation [51] which indicates that microwave energy favors an anisotropic growth caused by the differences in the surface energies on the different crystallographic faces [52]. Possibly, the imperfections or differences between the

height and width of these particles can be associated with the influence of microwave energy during the phase growth process. By roughly estimation and using the Sherrer formula, it was found that the individual particle size was approximately 30 nm.

An edge of the agglomerate shown in FEG-SEM was selected and characterized by means of HRTEM and SAED. From Fig. 4a we can see that the diameter of most particles is about 10–25 nm that is close to the average particle size estimated by XRD patterns. It is noteworthy that the synthesized particles are well dispersed. In fact, as we known, the powders produced by the microwave assisted method directly cannot prevent the aggregation without the help of dispersing agent or any following heat treatment [53–55]. In general, in the microwave assisted process, the smaller particles usually owe higher surface energy that makes them more easily to aggregate together once the microwave field is a union of magnetic field and electric field changing their direction at a frequency of 2.45 GHz. Figure 4b shows the SAED micrograph of the prepared particles. All the diffraction circles belong to spinel structure confirming that the product is $ZnFe_2O_4$, what is consistent to the result of XRD. The diffraction circles composed of lots of bright spots, suggesting that the particles are very small and with well-ordered crystalline structure. The perfect crystalline is mainly induced by the high-volume heating effect of microwave that make the atoms including that are in bridge arrange at an order.

The average diameter particle size (Fig. 5a) was determined to be around 500 nm. Also, we can observe particle agglomerates having a mean particle size of 30 nm. The as-synthesized spinel ferrite were relatively spherical with uniform size distribution. Sample porosity was tested by N2 adsorption–desorption isotherm, shown in Fig. 5b. The adsorption isotherm reveals little difference in the porosity of the particles as a function of the heterogeneous morphology. According to IUPAC (International Union of Pure and Applied Chemistry), the observed isotherms is classified as

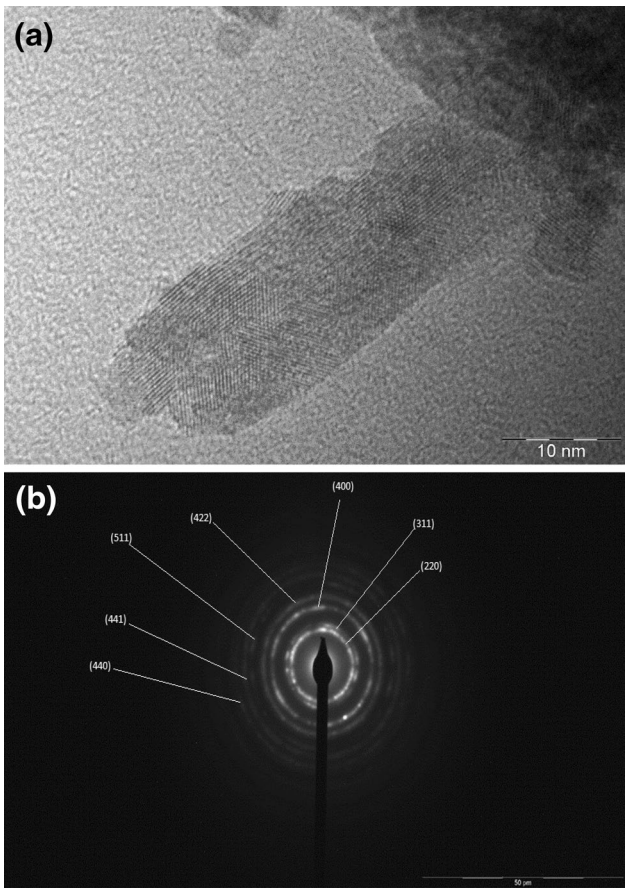

Fig. 4 **a** HR-TEM (high resolution-TEM) image of $ZnFe_2O_4$ nanoparticle synthesized at 140 °C for 32 min using the microwave assisted hydrothermal method and **b** SAED image of $ZnFe_2O_4$ nanoparticle synthesized at 140 °C for 32 min using the microwave assisted hydrothermal method

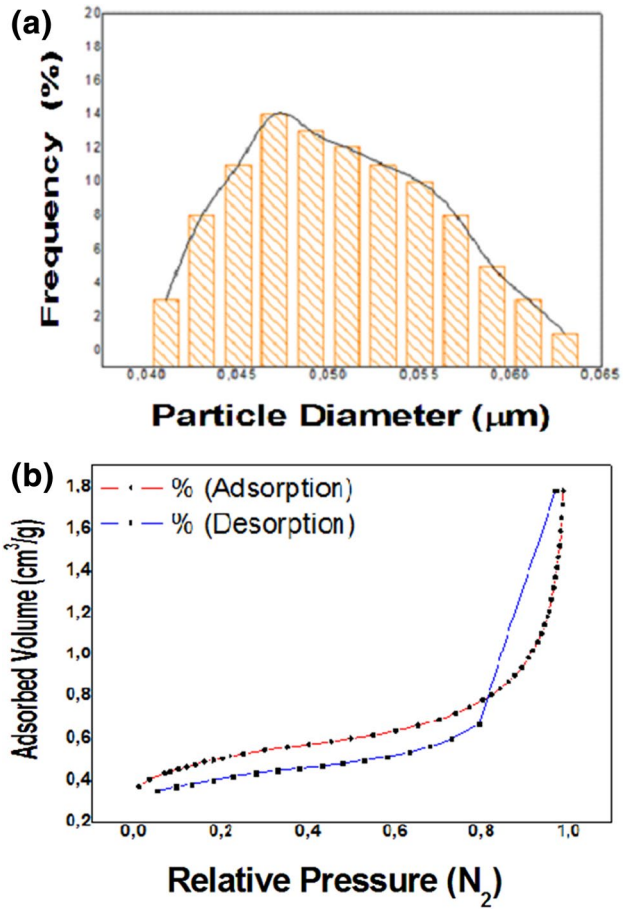

Fig. 5 **a** Particle size distribution of $ZnFe_2O_4$ nanoparticle synthesized at 140 °C for 32 min using the microwave assisted hydrothermal method and **b** N_2 adsorption–desorption isotherms for $ZnFe_2O_4$ nanoparticle synthesized at 140 °C for 32 min using the microwave assisted hydrothermal method

type III which is marked by a large volume of gas adsorbed at relative high pressures [56]. It is noted that the adsorption–desorption isotherm involves a small volume of gas. No hysteresis phenomenon is observed indicating that the particles are not porous or have closed cylindrical pores at one end.

Magnetic hysteresis loop (M.H. loop) was recorded employing the VSM. Figure 6 shows the hysteresis loops of the $ZnFe_2O_4$ nanoparticles recorded at room temperature. The coercivities of $ZnFe_2O_4$ nanoparticles is almost negligible and the remanent magnetization (Mr) of 2.3 emu/g. Thus the results clearly indicate the superparamagnetic behavior of the prepared samples due to decrease in the particle size below a critical value (lower than 50 nm) [57]. With an applied magnetic field around 3700 Oe the observed magnetization (Ms) value is 12.1 emu/g. The size of the crystalline nature influences the magnetic properties of the nanoparticles. Internal field can be generated due to the asymmetric distribution of oxygen vacancies. This effect induces complexes dipoles alignment and asymmetric distribution of oxygen vacancies, i.e.; positively oxygen vacancies (Vo°°) near negative electrode that holds electrons close to positive electrode. The spins of Fe^{3+}ions are aligned antiferromagnetically through a strong superexchange interaction as the angle Fe^{3+}–O^{2-}–Fe^{3+} is 180°. In $ZnFe_2O_4$, Fe^{3+} ions have a distorted octahedral local environment and the distortion causes a tilting of the octahedron from the direction of C-axis. In this study, the magnetization non-linearly increased with the applied magnetic field, which is characteristic of antiferromagnets. This behavior ruled out the presence of any dominating paramagnetic particles in the sample. The non-linear curve is typical of ferri/ferromagnetic type of variation where the magnetization slowly approaches saturation. Usually, such compound shows the paramagnetic nature at room temperature owing to its normal spinel structure. However, the coupling between the cations at both octahedral and tetrahedral sites can giving rise to occurrence of superparamagnetic behavior. $ZnFe_2O_4$ nanostructures obtained by the microwave assisted method could be ascribed to the presence of smaller primary nanocrystals which assembled together to generate different morphologies. During the hydrothermal treatment, if the temperature and pressure conditions are carefully maintained during the duration of the experiment, neither etching of spinel crystals nor the formation of a second phase is observed, as previously detected by XRD. The agglomeration process was attributed to Van der Waals forces. The random aggregation process between the small particles can be related to an increase in effective collision rates between small particles by microwave radiation which indicates that microwave energy favors an anisotropic growth caused by the differences in the surface energies on the different crystallographic faces. Possibly, the imperfections or differences between the height and width of these particles can be associated with the influence of microwave energy during the phase growth process. In this context, we suggested that the ratio $S=Mr/Ms$ could be used as a functionally parameter for evaluating the limit of single domain size of the magnetic nano-sized powder materials. That is why our nanoparticles obtained by HTMW can have multiple domain sizes and *Hc, Mr, S* will differ from zero. Once the coercive field differs from zero and open hysteresis loop is observed in combination with high magnetization, we expected that the ferromagnetic transition temperature will be above the room temperature. Therefore, we pretend to perform a deep study on the magnetic properties of pure zinc ferrite as a function of temperature, frequency, and other physical properties aiming to achieve reasonable characteristics for application in magnetohyperthermia.

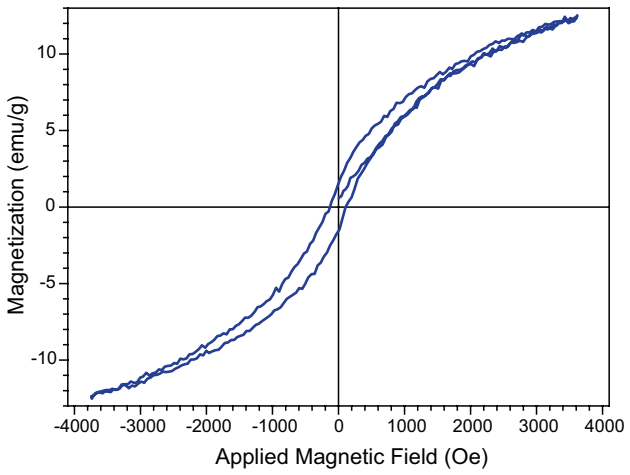

Fig. 6 *M-H* loop of $ZnFe_2O_4$ nanoparticle synthesized at 140 °C for 32 min using the microwave assisted hydrothermal method

4 Conclusions

Superparamagnetic $ZnFe_2O_4$ nanoparticles were successfully prepared by hydrothermal method without the use of any surfactant. The powder XRD analysis revealed the presence of the $ZnFe_2O_4$ belonging to face centered regular spinel cubic structure. FEG-SEM images exhibit agglomerated bunch of square shaped $ZnFe_2O_4$ nanoparticles. VSM measurements confirmed the superparamagnetic behavior of the synthesized samples at room temperature and the effect of crystallite size on the magnetic properties. Thus the present work concludes that the hydrothermal microwave assisted method has influence on the particle size and hence the properties of the $ZnFe_2O_4$ nanoparticles. The hydrothermal reaction to grow $ZnFe_2O_4$ crystallites is described by the dissolution–crystallization process. These

nanoparticles have interesting physical properties, such as adequate magnetization saturation values which make appropriate and possible use in hyperthermia. HTMW is important not only for the use of a short treatment time and low temperature but also for the possibility to control the morphological and structural properties. Therefore, the HTMW method is undeniably a genuine technique for low temperatures and short times in comparison with the previous methodologies.

Acknowledgements The financial support of this research project by the Brazilian research funding agency FAPESP (2016/02180-4) is gratefully acknowledged.

References

1. INCA, *Estimativa\2014: incidência de câncer no Brasil* (Instituto Nacional de Câncer José Alencar Gomes da Silva. Coordenação-Geral de Prevenção e Vigilância, INCA, Rio de Janeiro, 2014)
2. R.A. Weinberg, *The Biology of Cancer CL* (Garland Science, New York, 2006)
3. P. Shubik, Vascularization of tumors: a review. J. Cancer Res. Clin. Oncol. **103**(3), 211–226 (1982)
4. E.D. Passos, *Síntese e Caracterização de Microesferas Magnéticas para Utilização em Hipertermia* (Dissertação (Mestrado em Materiais)—Universidade Federal de Itajubá, Itajubá, 2006)
5. B. Djulbegovíc, C. Livingstone, *Decision-Making in Oncology: Evidence-Based Management*, 1st edn. (Churchill Livingstone, New York, 1997)
6. J. Overgaard, M. Overgaard, Hyperthermia as an adjuvant to radiotherapy in the treatment of malignant melanoma. Int. J. Hyperth. **3**, 483–501 (1987)
7. S. Klahr, Oxygen radicals and renal diseases. Miner. Electrol. Metab. **23**(3), 40–43 (1997)
8. Q.A. Pankhurst, J. Connoly, S.K. Jones, J. Dobson, Applications of magnetic nanoparticles in biomedicine. J. Phys. D **36**, 167–181 (2003)
9. S. Mornet, S. Vasseur, F. Grasset, E. Duguet, Magnetic nanoparticle design for medical diagnosis and therapy. J. Mater. Chem. **14**, 2161–2175 (2004)
10. J.M. IM, H.J. YOU, Y.S. YOON, D.W. SHIN, Synthesis of nanocrystalline $Gd_{0.1}Ce_{0.9}O_{2-x}$ for IT-SOFC by aerosol flame deposition. Ceram. Int. **34**(4), 877–881 (2007)
11. V.F. Castro, J. Celestino, A.A. Queiroz, F.G. Garcia, Propriedades magnéticas e biocompatíveis de nanocompósitos para utilização em magneto-hipertermia. Revista Brasileira de Física Médica **4**(1), 79–82 (2010)
12. J.A. Gomes, G.M. Azevedo, J. Depeyrot, J. Mestnik-Filho, G.J. Da Silva, F.A. Tourinho, R. Perzynski, $ZnFe_2O_4$ nanoparticles for ferrofluids: a combined XANES and XRD study. J. Magn. Magn. Mater. **323**, 1203 (2011)
13. P.A. Vinosha, L.A. Mely, J.E. Jeronsia et al., Synthesis and properties of spinel $ZnFe_2O_4$ nanoparticles by facile co-precipitation route. Optik **134**, 99–108, (2017)
14. Z.Ž. Lazarević, Č. Jovalekić, V.N. Ivanovski et al., Characterization of partially inverse spinel $ZnFe_2O_4$ with high saturation magnetization synthesized via soft mechanochemically assisted route. J. Phys. Chem. Solids **75**, 869–877 (2014)
15. C.M. Hurd, Varieties of magnetic order in solids. J. Contemp. Phys. **23**(5), 469–493 (1982)
16. P. Urbanowicz, E. Tomaszewicz, T. Gron et al., Superparamagnetic-like behavior and spin-orbit coupling in (Co,Zn) $RE_4W_3O_{16}$ tungstates (RE = Nd, Sm, Eu, Gd, Dy and Ho). J. Phys. Chem. Solids **72**, 891–898 (2011)
17. S. Bedanta, W. Kleemann, Superparamagnetism. J. Phys. D **42**(1), 013001, 2008
18. M. Venkatesan, C.B. Fitzgerald, J.M.D. Coey, Thin films: unexpected magnetism in a dielectric oxide. Nature **7000**, 630–630 (2004)
19. Y.S. Fu, X. Wang, Magnetically separable $ZnFe_2O_4$–graphene catalyst and its high photocatalytic performance under visible light irradiation. Ind. Eng. Chem. Res. **50**, 7210–7218 (2011)
20. A. Pradeep, P. Priyadharsini, G. Chandrasekaran, Structural, magnetic and electrical properties of nanocrystalline zinc ferrite. J. Alloy. Compd. **509**, 3917–3923 (2011)
21. M. Azharkhan, High frequency dielectric response and magnetic studies of $Zn_{1-x}Tb_xFe_2O_4$ nanocrystalline ferrites synthesized via micro-emulsion technique. J. Magn. Magn. Mater. **360**, 188–192 (2014)
22. D. Varshney, K. Verma, A. Kumar, Structural and vibrational properties of $Zn_xMn_{1-x}Fe_2O_4$ (x = 0. 0, 0. 25, 0. 50, 0. 75, 1.0) mixed ferrites. Mater. Chem. Phys. **131**, 413–419 (2011)
23. P. Laokul, Characterization and magnetic properties of nanocrystalline $CuFe_2O_4$, $NiFe_2O_4$, $ZnFe_2O_4$ powders prepared by the Aloevera extract solution. Curr. Appl. Phys. **11**, 101–108 (2011)
24. M.M. Rahman, Highly sensitive formaldehyde chemical sensor based on hydrothermally prepared spinel $ZnFe_2O_4$ nanorods. Sens. Actuators B **171**, 932–937 (2012)
25. T. Marinca, Structural and magnetic properties of nanocrystalline $ZnFe_2O_4$ powder synthesized by reactive ball milling. Optoelectron. Adv. Mater. Rapid Commun. **5**(1), 149–152, 2011
26. Z.W. Wang, P. Lazor, S.K. Saxena, G. Artioli, High pressure Raman spectroscopic study of spinel ($ZnCr_2O_4$). J. Solid State Chem. **165**, 165–170 (2002)
27. H. Zhang, X. Fu, S. Niu, Q. Xin, Synthesis and luminescent properties of nanosized YVO_4: Ln (Ln = Sm, Dy). J. Alloys Compd. **457**, 61–65 (2008)
28. H.S.C. O'neill, Temperature dependence of the cation distribution in zinc ferrite ($ZnFe_2O_4$) from powder XRD structural refinements. Eur. J. Mineral. **4**, 571–580 (1992)
29. A.Z. Simões, B.D. Stojanovic, M.A. Ramirez, A.A. Cavalheiro, E. Longo, J.A. Varela, Lanthanum-doped $Bi_4Ti_3O_{12}$ prepared by the soft chemical method: Rietveld analysis and piezoelectric properties. Ceram. Int. **34**, 257–261 (2008)
30. Z.V. Gabbasova, M.D. Kuz'min, A.K. Zvezdin, I.S. Dubenko, V.A. Murashov, D.N. Rakov, I.B. Krynetsky, $Bi_{1-x}R_xFeO_3$ (R = Rare earth): a family of novel magnetoelectrics. Phys. Lett. A **158**, 491–498 (1991)
31. A.V. Zalesskii, A.A. Frolov, T.A. Khimich, A.A. Bush, Composition-induced transition of spin-modulated structure into a uniform antiferromagnetic state in a $Bi_{1-x}La_xFeO_3$ system studied using 57Fe NMR. Phys. Solid State **45**, 134–138 (2003)
32. D. Lee, M.G. Kim, S. Ryu, H.M. Jang, S.G. Lee, Epitaxially grown La-modified $BiFeO_3$ magnetoferroelectric thin films. Appl. Phys. Lett. **86**, 222903–222905 (2005)
33. J. Li et al., Influence of Mn and Nb dopants on electric properties of chemical-solution-deposited $BiFeO_3$ films. Appl. Phys. Lett. **84**, 5261–5263 (2004)
34. H. Wang, J.J. Zhu, J.M. Zhu, X.H. Liao, S. Xu, T. Ding, Fabrication of porous metal oxides for catalytic applications using templating techniques. Phys. Chem. **4**, 3794–3799, 2002
35. G.J. Wilson, A.S. Matijasevich, D.R.G. Mitchell,, J.C. Schulz, G.D. Will, Modification of TiO_2 for enhanced surface properties: finite Ostwald ripening by a microwave hydrothermal process. Langmuir **22**, 2016–2027 (2006)

36. D.K. Agrawal, Microwave processing of ceramics. Curr. Opin. Solid State Mater. Sci. **3**, 480–486 (1998)
37. T. Tangcharoen, A. Ruangphanit, W. Pecharapaa, Structural and magnetic properties of nanocrystalline zinc-doped metal ferrites (metal = Ni; Mn; Cu) prepared by sol-gel combustion method. Ceram. Int. **39**, 239–243 (2013)
38. R. Rameshbabu, R. Ramesh, S. Kanagesan, A. Karthigeyan, S. Ponnusamy, Synthesis and study of structural, morphological and magnetic properties of $ZnFe_2O_4$ nanoparticles. J. Supercond. Nov. Magn. **27**, 1499–1502 (2014)
39. P.M.P. Swamy, S. Basavaraja, A. Lagashetty, N.S. Rao, R. Nijagunappa, A. Venkataraman, Synthesis and characterization of zinc ferrite nanoparticles obtained by self-propagating low-temperature combustion method. Bull. Mater. Sci. **34**(7), 1325–1330 (2011)
40. E. Shi, C.T. Xia, W.Z. Zhong, B.G. Wang, C.D. Feng, Crystallographic properties of hydrothermal barium titanate crystallites. J. Am. Ceram. Soc. **80**, 1567–1572 (1997)
41. Y.B. Khollam, A.S. Deshpande, A.J. Patil, H.S. Potdar, S.B. Deshpande, S. Date, Microwave-hydrothermal synthesis of equiaxed and submicron-sized $BaTiO_3$ powders. Mater. Chem. Phys. **71**, 304–308 (2001)
42. J. Yoo, The effects of microstructure on $Ba_{1-x}Sr_xTiO_3$ pyroelectric materials for pyroelectric and bolometer infrared sensors. Ph. D. Thesis, University of Auckland, 1999
43. A.Z. Simões, E.C. Aguiar, A.H.M. Gonzalez, J. Andrés, E. Longo, J.A. Varela, Strain behavior of lanthanum modified $BiFeO_3$ thin films prepared via soft chemical method. J. Appl. Phys. **104**, 104115-1–104115-6 (2008)
44. A. Z. Simões, L.S. Cavalcante, C.S. Riccardi, J.A. Varela, E. Longo, Improvement of fatigue resistance on La modified $BiFeO_3$ thin films. Curr. Appl. Phys. **9**, 520–523 (2009)
45. A.Z. Simões, M.A. Ramírez, C.S. Riccardi, E. Longo, J.A. Varela, Ferroelectric characteristics of $SrBi_4Ti_4O_{15}$ thin films grown on $Pt/Ti/SiO_2/Si$ substrates by the soft chemical method. Mater. Lett. **60**, 2020–2023 (2006)
46. A.Z. Simões, M.A. Ramírez, C.S. Riccardi, A.H.M. Gonzalez,, E. Longo, J.A. Varela, Synthesis and electrical characterization of $CaBi_2Nb_2O_9$ thin films deposited on $Pt/Ti/SiO_2/Si$ substrates by polymeric precursor method. Mater. Chem. Phys. **98**, 203–206 (2006)
47. A.Z. Simões, A.H.M. Gonzalez,, E.C. Aguiar, C.S. Riccardi, E. Longo, J.A. Varela, Piezoelectric behavior of $SrRuO_3$ buffered lanthanum modified bismuth ferrite thin films grown by chemical method. Appl. Phys. Lett. **93**, 142902–142904 (2008)
48. A.Z. Simões, C.S. Riccardi, L.S. Cavalcante, J.A. Varela, E. Longo, Size effects of polycrystalline lanthanum modified $Bi_4Ti_3O_{12}$ thin films. Mater. Res. Bull. **43**, 158–167 (2008)
49. A.Z. Simões, M.A. Ramírez, A.H.M. Gonzalez, C.S. Riccardi, A. Ries, E. Longo, J.A. Varela, Control of retention and fatigue-free characteristics in $CaBi_4Ti_4O_{15}$ thin films prepared by chemical method. J. Solid State Chem. **179**, 2206–2211, 2006
50. S.-J.L Kang, *Sintering Densification, Grain Growth and Microstructure* (Elsevier, Oxford, 2005)
51. M. Godinho, C. Ribeiro, E. Longo, E.R. Leite, Influence of microwave heating on the growth of gadolinium-doped cerium oxide nanorods. Cryst. Growth Des. **8**, 384–386 (2008)
52. J. Geng, Y. Lv, D. Lu, J.-J. Zhu, Sonochemical synthesis of $PbWO_4$ crystals with dendritic, flowery and star-like structures. Nanotechnology **17**, 2614–2620 (2006)
53. B. Hosni, Structure and electro chemical hydrogen storage properties of Ti_2Ni alloy synthesized by ball-milling. J. Alloys Compd. **615**, 119–125 (2014)
54. S.D. House, Effect of ball-milling duration and dehydrogenation on the morphology, microstructure and catalyst dispersion in Ni-catalyzed MgH_2 hydrogen storage materials, Acta Mater. **86**, 55–68 (2015)
55. R.M. Rahul, Enhanced lithium storage in $ZnFe_2O_4$–C nanocomposite produced by allow-energy ball-milling. J. Power Sources **282**, 462–470 (2015)
56. C.V. Santilli, S.H. Pulcinelli, Análise da textura de materiais cerâmicos a partir das isotermas de adsorção de gases. Cerâmica **39**(259), 11–16 (1993)
57. O.M. Lemine, Synthesis, structural, magnetic and optical properties of nano-crystalline $ZnFe_2O_4$. Phys. B **406**, 1989–1994 (2011)